RESEARCH ARTICLE
PLANETARY SCIENCES

Earth and Planetary Physics
10: 400–409, 2026
doi: 10.26464/epp2026038

Topography-induced flows in a sidewall-modified, rapidly rotating and precessing cylinder

XiuYu Chen[1,2], ChangShun Liu[1], LiGang Li[1*], and DaLi Kong[1*]
[1]Shanghai Astronomical Observatory, Chinese Academy of Sciences, Shanghai 200030, China;
[2]University of Chinese Academy of Sciences, Beijing 100049, China

Key Points:

- Finite-element simulations are performed for viscous incompressible flows in a rapidly rotating and precessing cylinder with sidewall topography.
- Introducing a vertical fin-type barrier along the sidewall substantially alters precessionally driven flow structures and enhances turbulence intensity.
- At high precession rates and large barrier heights, sidewall topography amplifies the flow's kinetic energy to unexpectedly high levels, potentially contributing to the maintenance of long-lived planetary magnetic fields.

Citation: Chen, X. Y., Liu, C. S., Li, L. G., and Kong, D. L. (2026). Topography-induced flows in a sidewall-modified, rapidly rotating and precessing cylinder. *Earth Planet. Phys.*, *10*(3), 400–409. http://doi.org/10.26464/epp2026038

Abstract: The influence of topography on rotating fluids may exceed conventional expectations. Here, we numerically examine viscous incompressible flows induced by sidewall topography, confined within a modified cylinder that rotates rapidly about its central vertical axis and precesses about another axis. To investigate specific flow patterns and boundary-interior correspondences, the cylindrical sidewall is modified by adding a vertical fin-type barrier extending all the way from the bottom to the top. The fully nonlinear Navier−Stokes equations with precessional forcing are solved in this modified cylindrical geometry, using a mixed finite element method. Numerical results show that the introduction of sidewall topography significantly alters the precessionally driven flow, particularly at high precession rates. While the primary dynamics associated with inertial wave propagation persist, rich vortical structures and turbulence emerge. Interestingly, the barrier does not invariably suppress the kinetic energy density; when its height approaches the cylinder radius under strong precession, the kinetic energy density even exceeds that of the cylinder case without a barrier. Such an anomalous enhancement of kinetic energy may offer new insights into how precession-driven flows over topography could contribute to sustaining long-lived planetary magnetic fields, including that of the early Moon.

Keywords: topography; precession; rotating flow; cylindrical geometry; inertial waves; turbulence; numerical simulation

1. Introduction

The influence of boundary topography on fluid dynamics has attracted considerable attention across a wide range of scientific and engineering disciplines. In geophysics, for instance, the Earth's core−mantle boundary (CMB) exhibits significant topographic irregularities, which play an essential role in the evolution of core and mantle dynamics (Lay et al., 1998). These irregularities can induce boundary-layer instabilities that are believed to cause various phenomena, such as enhanced core−mantle coupling, alterations in core convection, and the modulation of dynamo processes (Garcia and Souriau, 2000; Vidal et al., 2024). In atmospheric and oceanic dynamics, it is well known that certain equatorially trapped shallow-water waves, e.g. Kelvin modes and Yanai modes, are protected by the underlying topography (Delplace et al., 2017). In industrial applications, such as the design of fuel tanks for highly maneuverable vehicles, aircraft, and spacecraft, the deliberate placement of internal obstacles (i.e., artificial topography) is used to mitigate unwanted fluid motions (Whitford, 2004). Collectively, these examples highlight the pervasive influence and practical importance of boundary topography in shaping fluid behavior.

In response to these diverse applications, many fundamental studies have been conducted to explore how topography influences fluid motion. To study the dynamo transition of an incompressible electrically conducting fluid in a Couette system, numerical simulations are performed with a rough inner boundary (Finke and Tilgner, 2012). The presence of boundary roughness enhances the boundary forcing and reduces the critical rotation rate for dynamo onset. Such a scenario is currently realized in experiments by means of baffles attached to the inner sphere of a spherical Couette device (Rojas et al., 2021). Inspired by the topologically protected states found in two-dimensional semiconductors, studies of three-dimensional viscous rotating convection in

First author: X. Y. Chen, xiuyuchen@shao.ac.cn
Correspondence to: L. G. Li, llg@shao.ac.cn
D. L. Kong, dkong@shao.ac.cn
Received 26 NOV 2025; Accepted 13 FEB 2026.

cylindrical containers have shown that nonlinear wall states can persist even in the presence of bulk turbulence, and remain robust when the cylinder's sidewall is partially truncated by a vertical rectangular barrier (Favier and Knobloch, 2020). In the above-mentioned numerical and experimental studies, boundary topography does not seem to change the primary characteristics of the bulk fluid motion. However, the latitudinal libration experiment (Chen XY et al., 2025) in a triaxial ellipsoid indicates that the turbulent boundary layer may be responsible for the onset of bulk turbulence, and that the influence of boundary topography should be considered more carefully.

In the present study, we investigate precessionally driven flows in a modified cylindrical geometry, where a vertical fin-type barrier is set up on the sidewall and its height is varied across simulations. Precession occurs when a rapidly rotating body experiences an external torque that perturbs its spin, causing its angular momentum to precess in the inertial frame of reference. Under weak precessional forcing, inertial modes can be excited in the rotating frame of reference (Wood, 1966; Manasseh, 1992; Meunier et al., 2008; Liao XH and Zhang K, 2012). In certain geometries such as spheres, cylinders, and ellipsoids, these precessionally-driven flows can become particularly strong when an inertial mode resonates with the precessional forcing (Kong DL et al., 2014, 2015; Jiang JF et al., 2015). The cylinder used in this study is deliberately chosen with an aspect ratio $\Gamma = 0.502559$, defined as the ratio of the cylinder radius to its height, which corresponds to the primary resonance of the inertial mode $\boldsymbol{u}_{111}$. The geometry is a circular cylinder equipped with a single sidewall-mounted vertical fin; its height is varied systematically across simulations, in a configuration similar to Favier and Knobloch (2020). Geophysically speaking, a circular cylinder mimics the Earth's tangent cylinder, an imaginary cylindrical region tangent to the inner-core equator and aligned with the Earth's rotation axis (Zhang K and Liao XH, 2017). A series of numerical simulations are performed to examine the evolution of precessionally driven flows within these sidewall-distorted cylinders, spanning regimes from quasi-linear to strongly nonlinear.

It should be emphasized that topographic coupling is not exclusively introduced by artificial barriers. Even in a smooth circular cylinder without internal obstacles, precessionally driven flows are constrained by the container geometry (Kong DL et al., 2015). The introduction of barriers disrupts this geometric smoothness by adding discontinuities (sharp edges and vertical walls), thereby strengthening boundary-driven effects. In this sense, fin-type barriers amplify geometry-driven boundary effects that are already present in the unmodified cylinder.

The paper is organized as follows. Section 2 describes the geometry and the dimensionless governing equations. Section 3 presents the finite-element method and the three-dimensional discretization of a topography-modified cylinder. Section 4 discusses the numerical results and phenomena. And the concluding remarks and future perspectives are given in the final section 5.

2. Governing Equations

A cylindrical container filled with viscous incompressible fluid is considered, which has a radius Γd and height d. The aspect ratio $\Gamma = 0.502559$ is chosen to be at the primary resonance of the inertial mode $\boldsymbol{u}_{111}$, where the triple subscripts (m, n, k) in $\boldsymbol{u}_{mnk}$ specify the azimuthal (m), vertical (n) and radial (k) wavenumbers, respectively (Zhang K and Liao XH, 2017; Kong DL et al., 2014). In a horizontal cross-section perpendicular to the central vertical axis, the sidewall topography of the cylinder is marked by a mountain-shaped smooth curvature that can be described by

$$\mathcal{R}(\phi) = \begin{cases} \Gamma - H\exp\left[1 + \dfrac{1}{\left(\dfrac{\phi - \phi_c}{\Delta\phi}\right)^2 - 1}\right], & \text{if } \phi_c - \Delta\phi < \phi < \phi_c + \Delta\phi, \\ \Gamma, & \text{elsewhere} \end{cases} \tag{1}$$

and illustrated in Figure 1, in which H is the height of the barrier, ϕ_c is the central location of the barrier in the azimuthal coordinate, and $\Delta\phi$ is the half-angle width of the barrier. In a three-dimensional view, the sidewall topography extends from the bottom to the top of the cylinder, forming a fin-type vertical barrier. The modified cylindrical container rotates rapidly with an angular velocity $\boldsymbol{\Omega}_0 = \Omega_0\hat{\boldsymbol{z}}$ along its positive z axis and precesses slowly about a different axis that is fixed in an inertial frame. The angle between the two axes is α_p.

The cylindrical coordinate system fixed to the container is employed to describe the fluid motion, with the unit vectors ($\hat{\boldsymbol{s}}$, $\hat{\boldsymbol{\phi}}$, $\hat{\boldsymbol{z}}$) defined in the container frame of reference. The origin of this cylindrical coordinate system is at the center of the bottom plane. The time-dependent precession vector $\boldsymbol{\Omega}_p$ can be expressed in the container frame by

$$\boldsymbol{\Omega}_p = |\boldsymbol{\Omega}_p|\left[\hat{\boldsymbol{s}}\sin\alpha_p\cos(\phi + \Omega_0 t) - \hat{\boldsymbol{\phi}}\sin\alpha_p\sin(\phi + \Omega_0 t) + \hat{\boldsymbol{z}}\cos\alpha_p\right], \tag{2}$$

and the overall angular velocity can be written as $\boldsymbol{\Omega} = \Omega_0\hat{\boldsymbol{z}} + \boldsymbol{\Omega}_p$. As a result, the incompressible Navier–Stokes equations that describe the flow in the container are

$$\begin{aligned} &\frac{\partial \boldsymbol{u}}{\partial t} + \boldsymbol{u}\cdot\nabla\boldsymbol{u} + 2\Big\{\hat{\boldsymbol{z}}\Omega_0 + |\boldsymbol{\Omega}_p|\left[\hat{\boldsymbol{s}}\sin\alpha_p\cos(\phi + \Omega_0 t)\right. \\ &\quad \left. - \hat{\boldsymbol{\phi}}\sin\alpha_p\sin(\phi + \Omega_0 t) + \hat{\boldsymbol{z}}\cos\alpha_p\right]\Big\} \times \boldsymbol{u} \\ &\quad = -\nabla p + \nu\nabla^2\boldsymbol{u} - 2\hat{\boldsymbol{z}}|\boldsymbol{\Omega}_p|\Omega_0 s\sin\alpha_p\cos(\phi + \Omega_0 t), \end{aligned} \tag{3}$$

$$\nabla\cdot\boldsymbol{u} = 0. \tag{4}$$

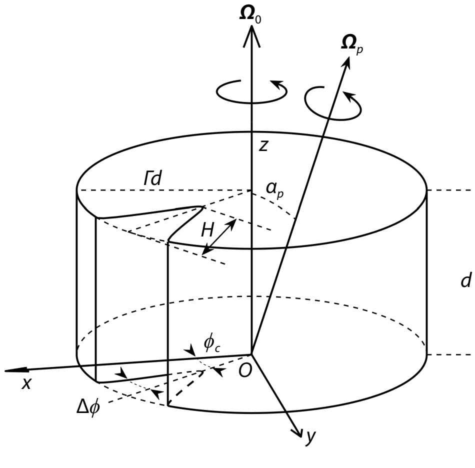

Figure 1. The sketch of an modified cylinder with a barrier.

In Equation (3), the last term on the right-hand side represents the Poincaré force which drives flows against viscous dissipation. The parameter ν denotes the kinematic viscosity. It should be noted that the reduced pressure p in this equation absorbs a time-dependent potential term $-sz|\boldsymbol{\Omega}_p|\Omega_0\sin\alpha_p\cos(\phi+\Omega_0 t)$. Equation (4) is the incompressibility condition. By adopting Ω_0^{-1} as the time scale, the height d as the length scale, and $\rho_0 d^2\Omega_0^2$ as the unit of pressure, the dimensionless equations read

$$\begin{aligned}\frac{\partial \boldsymbol{u}}{\partial t} &+ \boldsymbol{u}\cdot\nabla\boldsymbol{u} + 2\Big\{\hat{\boldsymbol{z}} + Po\big[\hat{\boldsymbol{s}}\sin\alpha_p\cos(\phi+t)\\ &-\hat{\boldsymbol{\phi}}\sin\alpha_p\sin(\phi+t)+\hat{\boldsymbol{z}}\cos\alpha_p\big]\Big\}\times\boldsymbol{u}\\ &= -\nabla p + Ek\nabla^2\boldsymbol{u} - 2\hat{\boldsymbol{z}}sPo\sin\alpha_p\cos(\phi+t),\end{aligned} \tag{5}$$

$$\nabla\cdot\boldsymbol{u} = 0, \tag{6}$$

where the Poincaré number $Po = |\boldsymbol{\Omega}_p|/|\boldsymbol{\Omega}_0|$ represents the relative strength of precession with respect to the rotation rate, and the Ekman number $Ek = \nu/(\Omega_0 d^2)$ measures the relative importance of viscous force compared with Coriolis force. In the container frame, the flow on the bounding surfaces of the modified cylinder is at rest, imposing

$$\boldsymbol{u} = \boldsymbol{0} \tag{7}$$

on the bottom $z = 0$, the top $z = 1$, and the sidewall $s = \mathcal{R}(\phi)$.

Note that the value of Ekman number depends on the choice of length scale. In this paper, the length scale is the height d of the cylinder. However, another typical choice of the length scale (e.g., Giesecke et al., 2019; Pizzi et al., 2021a) can be the radius of the cylinder. Because the aspect ratio Γ in this paper is about 0.5, the difference in the value of Ekman number caused by different length scales is by a factor of about 4. As a result, the adopted Ekman number 10^{-4} in Giesecke et al. (2019) is equivalent to $Ek = 2.5\times10^{-5}$ of the present study. Although the value of Ekman number is not our primary concern, it indeed affects the dimensionless amplitude of the resonant flow. The critical precession forcing (the critical Po number), which characterizes the transition from a more laminar flow to a turbulent flow, shifts to smaller values when decreasing Ek.

3. Mixed Finite-element Methods and Numerical Computations

The time integration for the numerical model engages a semi-implicit, second-order, uniform time-step backward differentiation formula (Ascher and Petzold, 1998; Chan KH et al., 2006),

$$\left(\frac{\partial \boldsymbol{u}}{\partial t}\right)^{n+1} = \frac{3\boldsymbol{u}^{n+1} - 4\boldsymbol{u}^{n} + \boldsymbol{u}^{n-1}}{2\Delta t} + O(\Delta t^2),$$

for the time derivative and

$$\boldsymbol{u}^{n+1}\cdot\nabla\boldsymbol{u}^{n+1} = (2\boldsymbol{u}^{n} - \boldsymbol{u}^{n-1})\cdot\nabla\boldsymbol{u}^{n+1} + O(\Delta t^2),$$

for the nonlinear term. The superscript n marks the n-th time step at which the time is $t_n = n\Delta t$ for $n = 0, 1, 2, \ldots$. The full temporal discretization of the dimensionless Navier–Stokes Equation (5)–(6) reads

$$\begin{aligned}\frac{3\boldsymbol{u}^{n+1} - 4\boldsymbol{u}^{n} + \boldsymbol{u}^{n-1}}{2\Delta t} &+ (2\boldsymbol{u}^{n} - \boldsymbol{u}^{n-1})\cdot\nabla\boldsymbol{u}^{n+1} + 2(\hat{\boldsymbol{z}} + Po\hat{\boldsymbol{\Omega}}_p^{n+1})\times\boldsymbol{u}^{n+1}\\ &= -\nabla p^{n+1} + Ek\nabla^2\boldsymbol{u}^{n+1} - 2Po\left[s\sin\alpha\cos(\phi+t_{n+1})\right]\hat{\boldsymbol{z}},\end{aligned} \tag{8}$$

$$\nabla\cdot\boldsymbol{u}^{n+1} = 0, \tag{9}$$

where

$$\hat{\boldsymbol{\Omega}}_p^{n+1} = \sin\alpha_p\left[\hat{\boldsymbol{s}}\cos(\phi+t_{n+1}) - \hat{\boldsymbol{\phi}}\sin(\phi+t_{n+1})\right] + \hat{\boldsymbol{z}}\cos\alpha_p. \tag{10}$$

Starting from arbitrary initial conditions, $\boldsymbol{u}^{n+1}$ can be successively determined from the known $\boldsymbol{u}^{n}$ and $\boldsymbol{u}^{n-1}$.

In order to solve Equations (8)–(9) subject to the boundary conditions Equation (7) at the time step $n+1$, the computational domain is discretized into tetrahedral elements using Netgen, an open-source mesh generator (Schöberl, 1997). It is flexible to put more nodes near the boundary for resolving the thin viscous boundary layer while retaining fewer bulk nodes in order to reduce computing loads. The typical mesh size, as illustrated in Figure 2, is therefore refined near the bounding surfaces but coarse in the interior domain. The total number of nodes in the mesh is about 2 million and these nodes make up about 1.5 million tetrahedral elements, which are sufficient for the numerical simulations at the Ekman number 10^{-4}.

A P2/P1 mixed finite element method (Stenberg, 1984) is employed, by which the velocity field is expanded into a piece-wise second-order polynomial by nodal quadratic bases defined on tetrahedral vertices and edge midpoints, while the pressure field is approximated by a piece-wise first-order function constructed by nodal linear bases defined on tetrahedral vertices. A saddle-point algebraic problem is obtained after the Galerkin weighted residual approach is applied (John, 2016). A stabilized Krylov subspace iterative solver (the stabilized BiCG) is used to solve the system of linear equations. The convergence property and numerical stability of the spatial discretization have been extensively demonstrated in Chan KH et al. (2010), Kong DL et al. (2015, 2014).

Without loss of generality, our simulations set the precession angle $\alpha_p = \pi/4$, the barrier location $\phi_c = \pi$ and half-width $\Delta\phi = \pi/20$. The Ekman number in most laboratory experiments and numerical simulations typically falls within the range of $10^{-5} \le Ek \le 10^{-4}$ (for example, Kobine, 1995; Meunier et al., 2008; Lin YF et al., 2014). As direct numerical simulations are computationally expensive, and since numerical solutions at $Ek = 10^{-5}$ or smaller show similar behavior to those at $Ek = 10^{-4}$, we choose a moderate value of $Ek = 10^{-4}$ for all simulations presented below.

4. The Influences of Sidewall Topography

We have carried out three groups of numerical simulations,

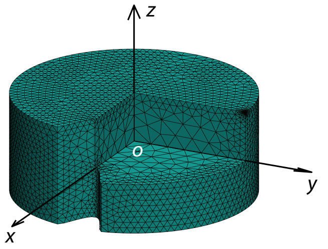

Figure 2. A sketch of the three-dimensional tetrahedralization of a cylinder with a barrier on the sidewall. The mesh is coarse in the interior and refined near the boundaries.

demonstrating the influences of the sidewall topography on precessionally-driven flows. The Poincaré number increases from small, to moderate, to large values across different groups, resulting in progressively more turbulent flow. In each group of simulations, the topographical distortions are imposed stronger and stronger by increasing the height H of the barrier.

4.1 A Perfect Cylinder without Sidewall Topography

In order to clarify the influence of sidewall topography, we first review the fundamental precessionally-driven flows in a perfect circular cylinder without any topography.

When the precession rate is small, $Po = O(10^{-4})$, in the perfect cylinder with aspect ratio $\Gamma = 0.502559$, the precessionally-driven flow can be decomposed into a series of inertial modes $\boldsymbol{u}_{mnk}$. The Poincaré force can resonate directly with the inertial mode $\boldsymbol{u}_{111}$ whose half-frequency is 0.5. Other modes are damped heavily by viscous dissipation (Kong DL et al., 2015). Figures 3a–3f show the retrograde wave in one propagating period by plotting the z component of the flow velocity in the $z = 1/2$ plane. Figures 3g–3h show, respectively, the axial component of the flow velocity $\hat{\boldsymbol{z}} \cdot \boldsymbol{u}$ and the helicity $h = \boldsymbol{u} \cdot \boldsymbol{\omega}$ in the perfect circular cylinder. Helicity quantifies the degree of alignment between the velocity ($\boldsymbol{u}$) and vorticity ($\boldsymbol{\omega} = \nabla \times \boldsymbol{u}$) fields, and is a key indicator for identifying the three-dimensional and complex structure of turbulent flows, such as helical motions and strong vortex interactions (Moffatt, 2014). In this study, helicity is used to assess the intensity and spatial distribution of turbulence under various precessional forcings and with barriers of different heights. The results shown in Figure 3h demonstrate that the interior flow primarily exhibits azimuthal motion, where the velocity is perpendicular to the vorticity ($\boldsymbol{u} \cdot \boldsymbol{\omega} = 0$). In contrast, at the top and bottom boundaries, and at the sidewall layer, the combined effects of precession and viscosity (Ekman boundary layers) introduce secondary flows with axial and radial velocity components. In these regions, enhanced alignment between velocity and vorticity leads to elevated local helicity, while the interior remains stable and nearly laminar.

When the Poincaré number gets large, e.g. $Po = 0.5$, the retrograde

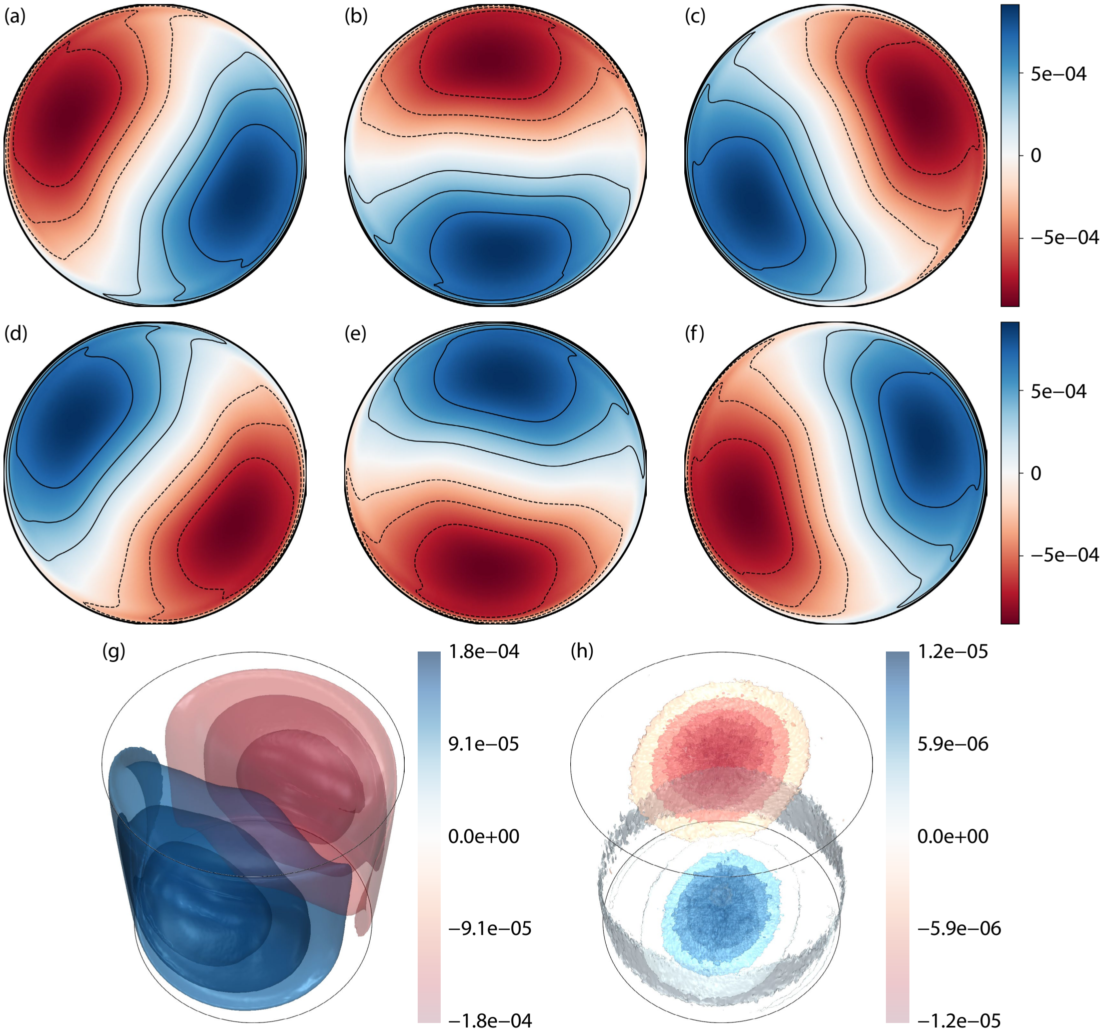

Figure 3. Precessionally driven flow in a perfect cylinder at $Po = 10^{-4}$. Panels (a)–(f) show contours of $\hat{\boldsymbol{z}} \cdot \boldsymbol{u}$ in the container frame on the plane $z = 1/2$ for $\Gamma = 0.502559$. Solid lines indicate positive contours and dashed lines indicate negative contours. Panels (a) to (f) depict the six sequential instants in one wave propagation period. The wave propagates westward (in the $-\hat{\phi}$ direction), i.e. retrograde. Further details are given in Kong DL et al. (2015). Panels (g) and (h) show the z component of the velocity field and the helicity, respectively, in the perfect cylinder at a specific instant.

traveling wave in the perfect cylinder is shown in Figures 4a–4f, where many modes are excited (Kong DL et al., 2014). The strongly forced flow is marked by a predominant axisymmetric geostrophic component (zonal flow) in the bulk volume of the cylinder plus a sidewall-localized shear layer. Figure 4g shows the z component of the flow velocity in the perfect cylinder, revealing clearly the presence of a sidewall localized shear layer. As shown in Figure 4h, the helicity is predominantly elevated in these sidewall regions, whereas the interior of the cylinder exhibits lower helicity. This distribution suggests that the flow near the sidewall is more complex, while the interior region remains comparatively quiescent and less structured. This numerical simulation is run for a sufficiently long time, and the overall structure of the strongly nonlinear flow appears to be highly stable.

4.2 Small Poincaré Number with Different Barrier Heights

When the Poincaré number is small, the flow is laminar, and the sidewall topography does not fundamentally alter the primary inertial mode. In Figures 5a–5c, three sub-figures are presented demonstrating the wave propagation with different barrier heights (multimedia views are available via the Supplementary Materials link). The barrier heights H are 0.1, 0.25 and 0.5 respectively. In the cases with small to moderate barrier heights, the overall fluid motion is not substantially affected. A barrier has a greater effect on the precessionally-driven flow only when the height almost reaches the radius of the cylinder container (as shown in Figure 5c (multimedia view)). The inertial mode is slightly distorted as it propagates around the barrier but largely returns to its undistorted pattern after it propagates away from the barrier. Boundary topography does not cause bulk turbulences. This can be seen from Figures 5d–5f (multimedia view), which demonstrate the helicity.

4.3 Moderate Poincaré Number with Different Barrier Heights

As the Poincaré number increases to $Po = 0.1$, the topographical influence of the boundary on precessionally-driven flow becomes more apparent. Even without a barrier, the original flow is moderately turbulent (Kong DL et al., 2015). The presence of the barrier, regardless of its height, intensifies the chaotic condition both near

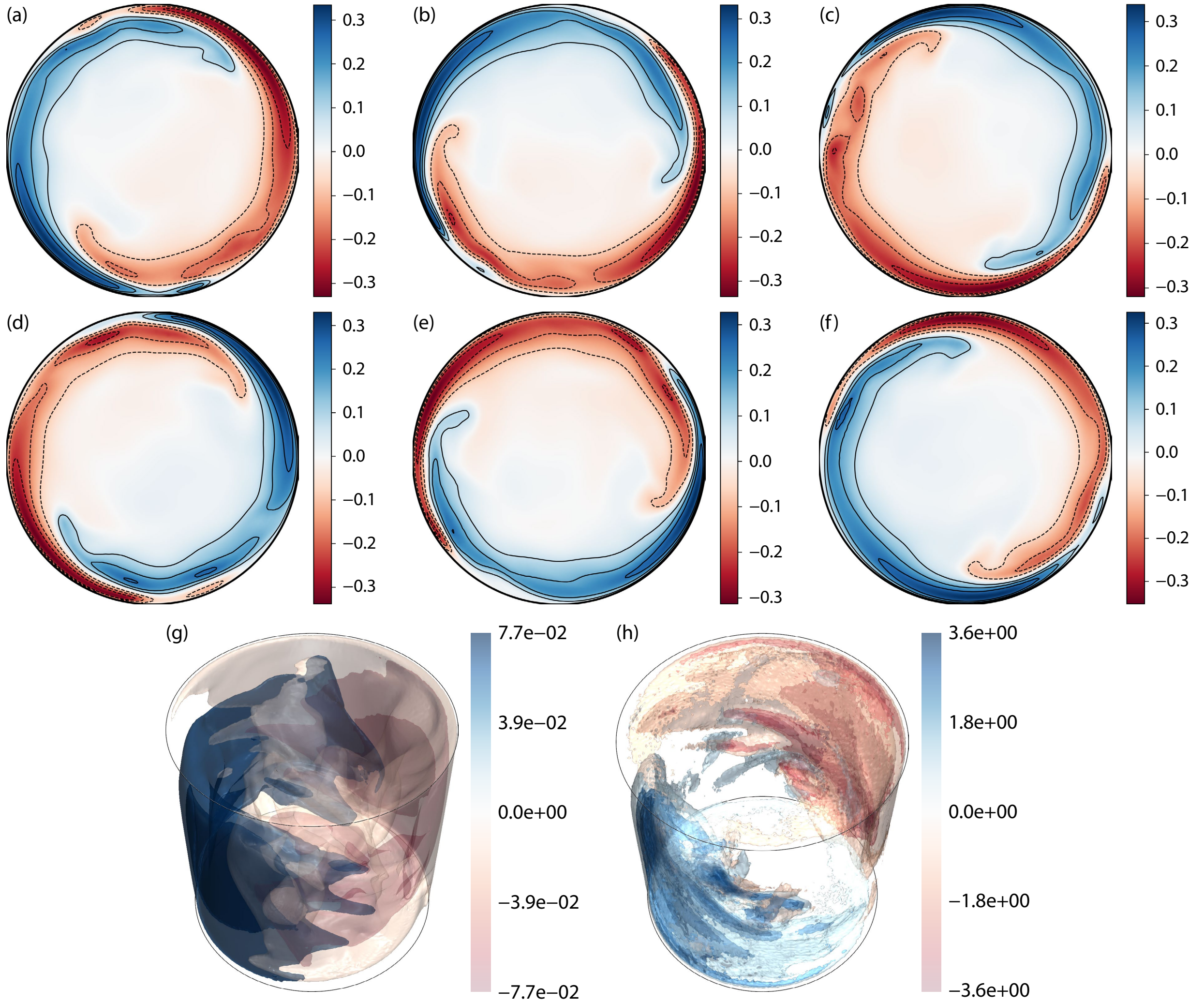

Figure 4. Precessionally driven flow in a perfect cylinder at $Po = 0.5$. Panels (a)–(f) show contours of $\hat{\boldsymbol{z}} \cdot \boldsymbol{u}$ in the container frame on the plane $z = 1/2$ for $\Gamma = 0.502559$. Panels (a) to (f) depict the six sequential instants in one wave propagation period. Panels (g) and (h) show the z component of the velocity field and the helicity, respectively, in the perfect cylinder at a specific instant.

the boundary and in the bulk, as shown in Figures 6a–6c (multimedia view). However, the propagating wave amplitude depicted by the $\hat{\boldsymbol{z}}\cdot\boldsymbol{u}$ component is suppressed at the leading side of the barrier (i.e., the side first encountered by the propagating wave). A major bulk vortex is formed at the trailing side of the barrier (i.e., the side downstream where the wave passes after interacting

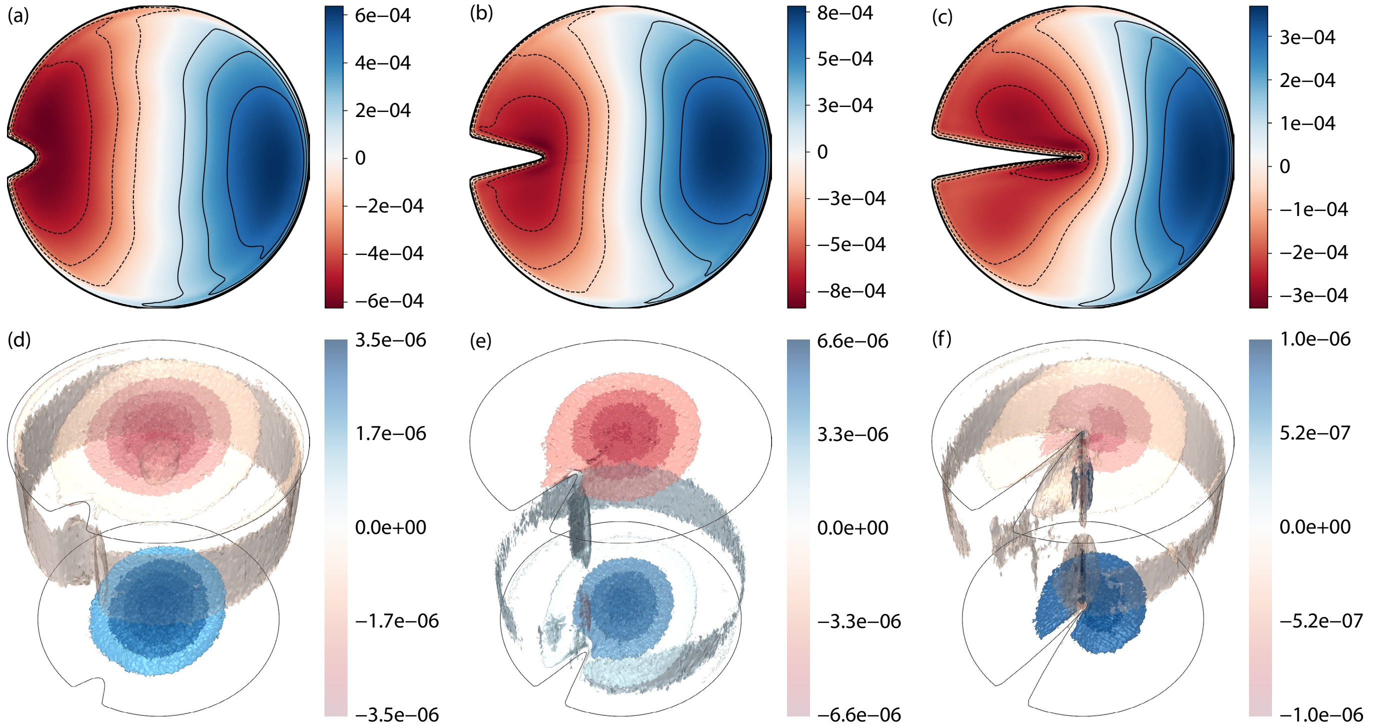

Figure 5. Precessionally driven flow in a cylinder with a barrier of different height at $Po = 10^{-4}$ ($\Gamma = 0.502559$). Panels (a)–(c) show contours of $\hat{\boldsymbol{z}}\cdot\boldsymbol{u}$ in the container frame on the plane $z = 1/2$ for barrier heights (a) $H = 0.1$, (b) $H = 0.25$, and (c) $H = 0.5$ (multimedia views). Panels (d)–(f) show instantaneous three-dimensional visualizations of the helicity for (d) $H = 0.1$, (e) $H = 0.25$, and (f) $H = 0.5$ (multimedia views).

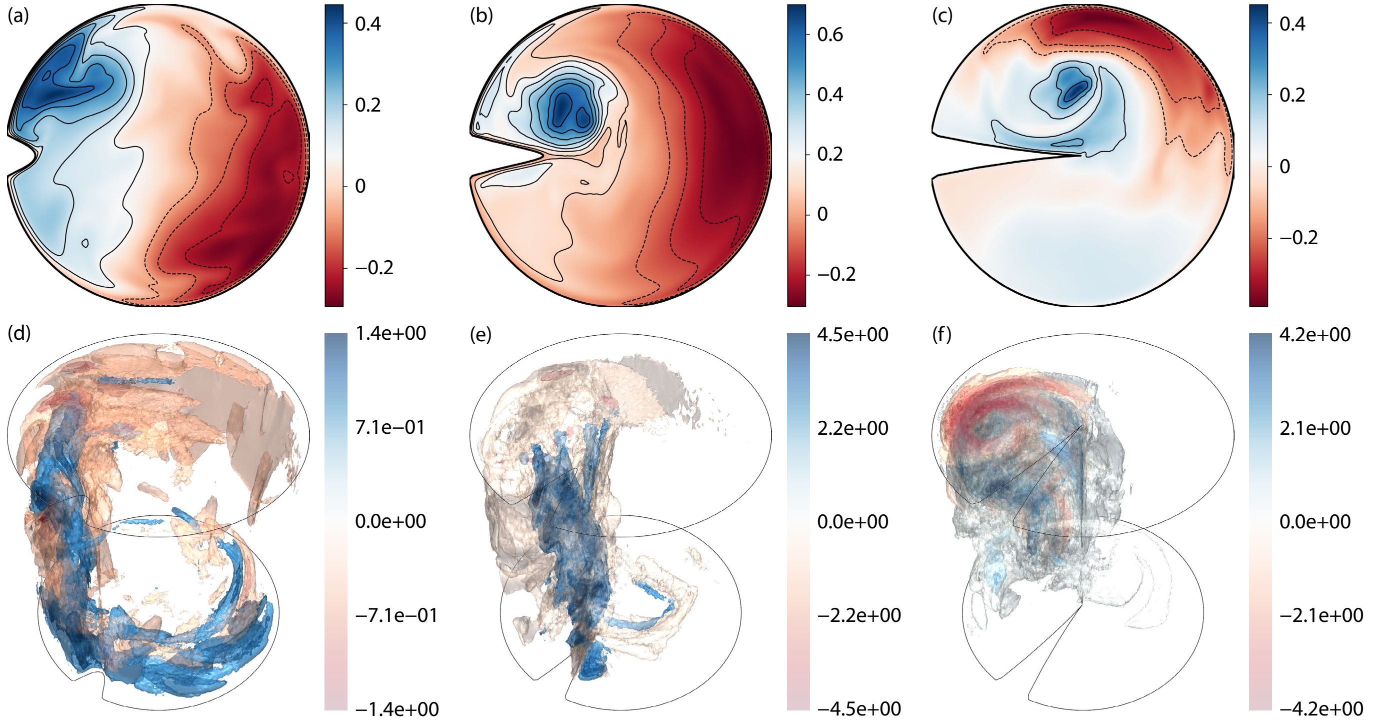

Figure 6. Precessionally driven flow in a cylinder with a barrier of different height at $Po = 0.1$ ($\Gamma = 0.502559$). Panels (a)–(c) show contours of $\hat{\boldsymbol{z}}\cdot\boldsymbol{u}$ in the container frame on the plane $z = 1/2$ for barrier heights (a) $H = 0.1$, (b) $H = 0.25$, and (c) $H = 0.5$ (multimedia views). Panels (d)–(f) show instantaneous three-dimensional visualizations of the helicity for (d) $H = 0.1$, (e) $H = 0.25$, and (f) $H = 0.5$ (multimedia views).

with the barrier), especially when the barrier height is larger than half of the radius of the cylinder, as shown in Figures 6d–6f (multimedia view). Through the animation of the helicity variations, it can be seen that the sign, strength and large-scale pattern of the trailing vortices are roughly stable and periodic in time.

4.4 Large Poincaré Number with Different Barrier Heights

As the precession rate gets really large to $Po = 0.5$, the strongly nonlinear waves are changed dramatically by sidewall barriers. Even a very short barrier can induce significant turbulence, as can be seen in Figure 7a (multimedia view) and Figure 7d (multimedia view). When the barrier becomes even taller, namely $H = 0.25$ and $H = 0.5$, the sidewall-localized wave (see Figures 4a–4f) is totally replaced by bulk turbulent flows, which are displayed in Figures 7b–7c (multimedia view) and Figures 7e–7f (multimedia view).

4.5 Downstream Modification of the u_z Structure by the Barrier

We further examine the flow in a vertical cross-section located immediately downstream of the barrier (Figure 8). Figure 8a shows the reference structure given by the axial component of the $\boldsymbol{u}_{111}$ mode, $\hat{\boldsymbol{z}} \cdot \boldsymbol{u}_{111}$. For a small Poincaré number and a finite

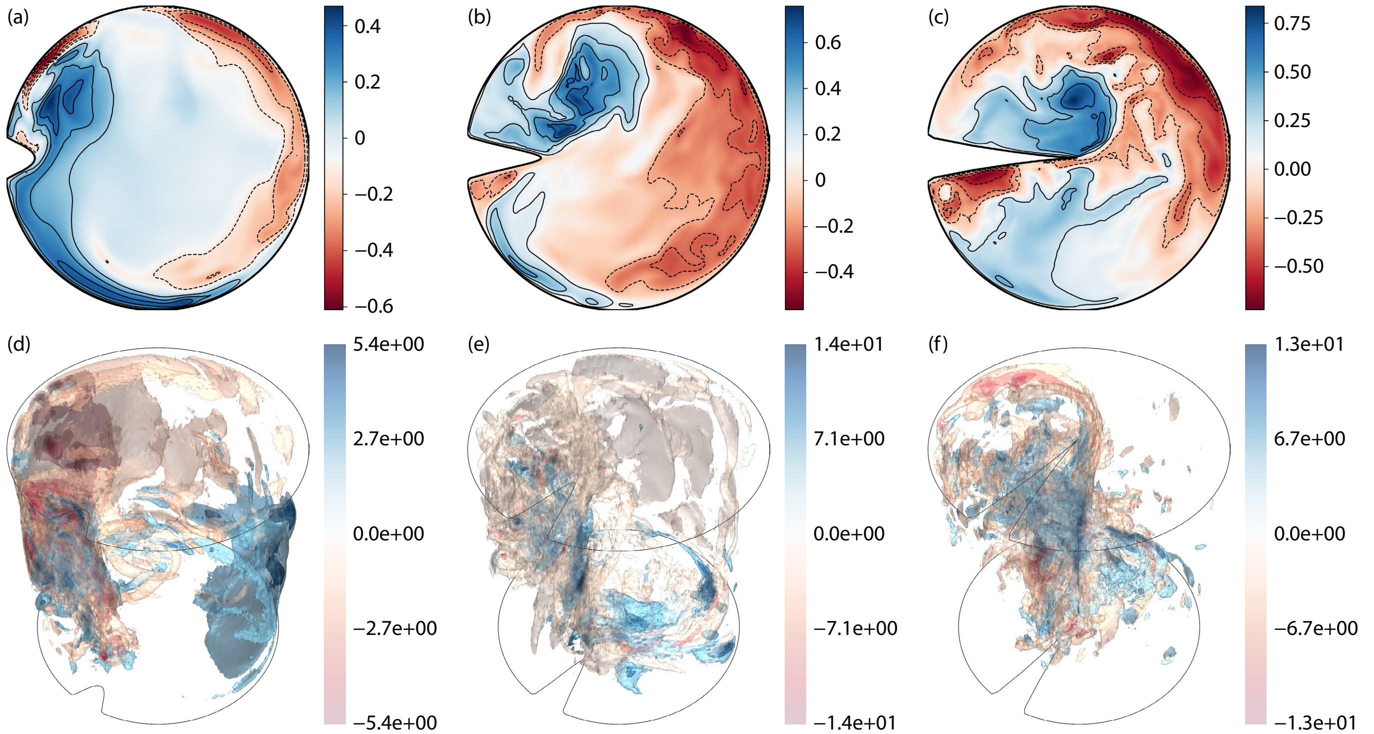

Figure 7. Precessionally driven flow in a cylinder with a barrier of different height at $Po = 0.5$ ($\Gamma = 0.502559$). Panels (a)–(c) show contours of $\hat{\boldsymbol{z}} \cdot \boldsymbol{u}$ in the container frame on the plane $z = 1/2$ for barrier heights (a) $H = 0.1$, (b) $H = 0.25$, and (c) $H = 0.5$ (multimedia views). Panels (d)–(f) show instantaneous three-dimensional visualizations of the helicity for (d) $H = 0.1$, (e) $H = 0.25$, and (f) $H = 0.5$ (multimedia views).

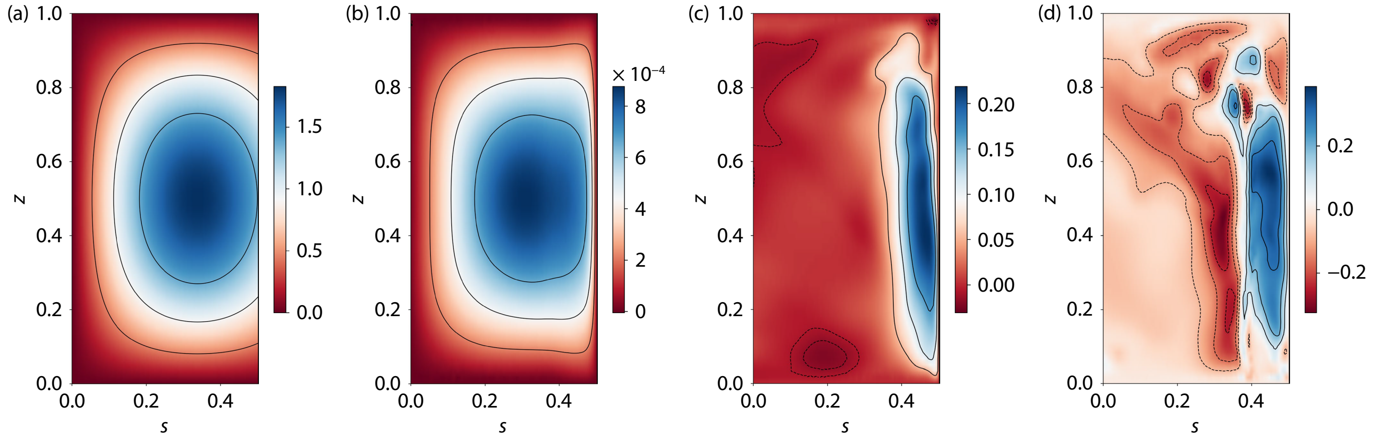

Figure 8. Axial velocity in a vertical cross-section at $\Delta\phi = 19\pi/20$, immediately downstream of the barrier. Panels (a) and (c) show results in a perfect cylinder, while panels (b) and (d) correspond to a cylinder with a barrier of height $H = 0.1$. Specifically, (a) $\hat{\boldsymbol{z}} \cdot \boldsymbol{u}_{111}$ in the perfect cylinder; (b) u_z with the barrier at $Po = 10^{-4}$ (multimedia view); (c) u_z in the perfect cylinder at $Po = 0.5$; and (d) u_z with the barrier at $Po = 0.5$ (multimedia view).

barrier height $H = 0.1$, the vertical pattern u_z is only weakly modified (Figure 8b), and remains largely consistent with the $\boldsymbol{u}_{111}$-dominated structure. This is also consistent with the Fourier-spectral analysis, in which the response is dominated by the forcing frequency.

As the Poincaré number increases to moderate and large values, the sidewall-localized structure observed in the perfect cylinder becomes increasingly perturbed by the barrier (Figure 8c–8d). Compared with the smooth, coherent pattern in Figure 8c, Figure 8d exhibits a more irregular, patchy structure with small-scale fluctuations. Likewise, the spectra extracted in the vicinity of the barrier are still dominated by the forcing frequency, but numerous secondary peaks emerge as Po increases, indicating that the flow has become fully turbulent. This suggests that the excitation of inertial waves may be associated with the formation of large-scale vortices at moderate and large Poincaré numbers.

4.6 Azimuthal Flow and Kinetic Energy Density

It is also interesting to look at the impact of sidewall topography on the flows both from their horizontal velocity and the perspective of kinetic energy density. For a perfect circular cylinder of $\Gamma = 0.502559$, increasing precession forcing leads to a strong westward ($-\hat{\phi}$ direction) axisymmetric geostrophic flow (Giesecke et al., 2019; Pizzi et al., 2021b; Gao DL et al., 2021). In this paper, the geometry is apparently non-axisymmetric, which prevents analysis based on inertial modes decomposition in the cylindrical volume (Kong DL et al., 2015). But because the geometric symmetry with respect to the middle plane ($z = 1/2$) remains, it is still sound to examine the horizontal flow component on the plane $z = 1/2$ for barrier-flow interplay. We focus on the azimuthal component of velocity, which represents the part of a flow that directly collides onto a sidewall barrier which should be strongly influenced by the existence of a barrier. Figure 9 plots the mean azimuthal flows that are defined as

$$U_\phi(s) = \frac{1}{\mu(A_s)}\int_{A_s} \hat{\phi}\cdot\boldsymbol{u}(s,\phi;z=1/2)\,\mathrm{d}\phi, \tag{11}$$

where

$$A_s = \{\phi \in [0,2\pi) : s \le \mathcal{R}(\phi)\}. \tag{12}$$

Here, A_s represents the set of all azimuthal angles ϕ at which the point (s,ϕ) remains inside the fluid domain, i.e., s does not exceed the local boundary $\mathcal{R}(\phi)$. The measure function

$$\mu(A_s) = \int_{A_s} \mathrm{d}\phi \tag{13}$$

gives the total angular span (in radians) where radius s lies inside the domain. In the case of a perfect circular cylinder without barrier, i.e., $\mathcal{R}(\phi) = \Gamma$ for any ϕ, we simply have $\mu(A_s) = 2\pi$ for all $s \le \Gamma$. Here, $\mu(A_s)$ denotes the total azimuthal length (in radians) for which points at radius s are within the cylinder.

It is apparent that a barrier impacts the generation of zonal circulation a lot. In the $H = 0.1$ case (see Figure 9a), the main feature of westward zonal flow and the trend of zonal flow saturation still can be seen. But for $Po = 0.5$, because the barrier is well higher than the thickness of the outer shear layer of the strongly forced flow, the weakening of the flow is obvious. With further increase of H, namely Figure 9b–9c, the nature of mean circulation changes fundamentally. There seems to be competition between the topography and precession. Large Po forcing still works hard to drive westward zonal flow, despite being suppressed, against the topographical resistance. But smaller Po forcing is unable to outweigh the obstacle, such that mean circulation can be reversed to eastward ($+\hat{\phi}$ direction) in the outer cylindrical region where barriers place azimuthal truncation. This feature can be seen in Figures 6–7, where vortices form downstream of the barrier.

The kinetic energy density of a flow can be defined by

$$E_{\mathrm{kin}} = \frac{1}{2V}\int_V |\boldsymbol{u}|^2\,\mathrm{d}V.$$

It measures the average strength of the flow. The dependence of E_{kin} on the Poincaré number Po in modified cylinders with different topography H is plotted in Figure 10 for the purpose of seeing the combined effect of precession and topography. The numerical simulation agrees well with the linear analytic results given by Zhang K and Liao XH (2017) in the perfect cylinder when $Po \le 0.01$. For example, direct nonlinear simulation yields $E_{\mathrm{kin}} = 1.6\times10^{-3}$ for $Po = 0.01$ at $Ek = 10^{-4}$, while the analytical expression gives $E_{\mathrm{kin}} = 1.9\times10^{-3}$ for $Po = 0.01$. However, when $Po > 0.01$, the nonlinear simulations show that E_{kin} gradually saturates and deviates from the linear theoretical prediction, which indicates that nonlinear effects become significant at larger Po.

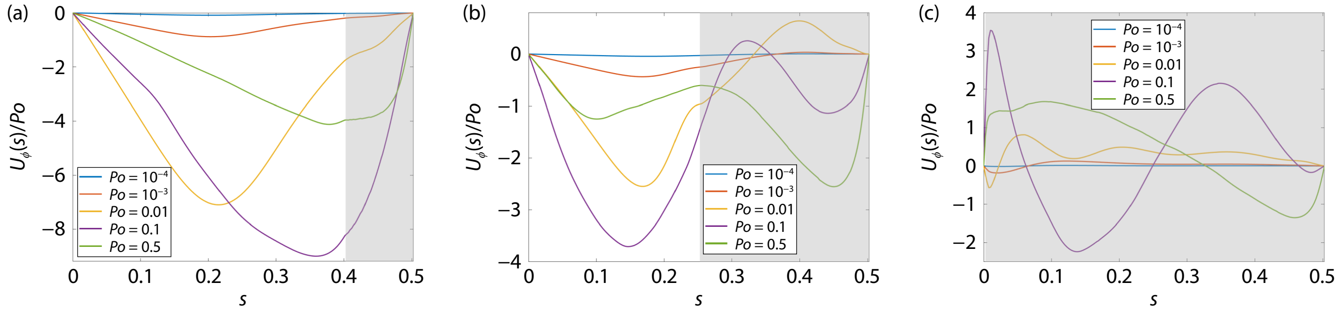

Figure 9. Mean azimuthal flow at the $z = 1/2$ plane, computed from Equation (11). The horizontal axis (s) represents the distance from the rotation axis, and the flow speed is re-scaled by Po. Panels (a)–(c) plot respectively cases of $H = 0.1$, $H = 0.25$ and $H = 0.5$. In each panel, the gray shaded region indicates the barrier's height measured from the sidewall of the cylinder. Note that for panel (c), since the barrier height $H = 0.5$, is nearly equal to the cylinder's aspect ratio, $\Gamma = 0.502559$, the shaded region extends close to the left vertical axis.

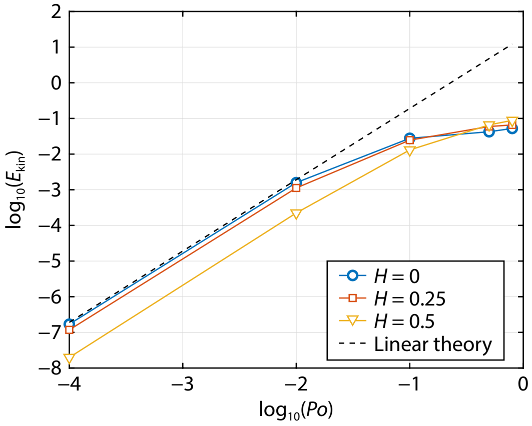

Figure 10. The kinetic energy density E_{kin} is plotted in logarithm scale as a function of the Poincaré number Po in cylinders with sidewall barriers of heights $H = 0$, $H = 0.25$ and $H = 0.5$ respectively. The dashed line represents the analytical expression of E_{kin} in the perfect cylinder, as given by Zhang K and Liao XH (2017). For visual clarity, the case $H = 0.1$ is omitted as it overlaps with the adjacent curves for $H = 0$ and $H = 0.25$.

Another interesting phenomenon is that, at weak to moderate precessional forcing (i.e., at the small Po end in Figure 10), increasing the height of the obstacle leads to a greater reduction in the flow strength. The trend becomes opposite when the precession gets strong. As demonstrated in Figure 10, towards the large Po end, higher barrier height H results in higher kinetic energy density. For example, at the large Po end, E_{kin} is 5.2×10^{-2} for $H = 0$, while it increases to 8.8×10^{-2} when $H = 0.5$. Under strong Poincaré forcing, topographical barriers on the cylindrical sidewall interact with the flow more vigorously, generating significant bulk turbulence through complex boundary processes (see the helicity's magnitude in Figure 7). In this regime, taller barriers enhance these turbulent interactions and drive more energetic flows, resulting in a noticeable increase in kinetic energy with barrier height. This suggests that, rather than damping the flow, high barriers can act as catalysts for turbulence and energy input when the precession is sufficiently strong.

5. Conclusions

In this paper, we have investigated the topographical influences of boundaries on fluid motions in rapidly rotating and precessing modified cylindrical containers via numerical experiments using 3D finite-element method. Compared with the precessionally driven flow in a perfect cylinder at the primary inertial-mode-resonance, which is mainly marked by a retrograde $m = 1$ wave propagation, the topographical effects resulting from modified cylindrical sidewalls are mainly found to be of three remarkable characteristics. First, a simple vertical barrier on the cylinder's sidewall will not fundamentally alter the large-scale $m = 1$ wave structure. The resonance between the Poincaré forcing and the $\boldsymbol{u}_{111}$ mode is robust under topographical perturbations. Second, the presence of a vertical barrier on the cylinder's sidewall can interact nonlinearly with precessionally-driven flows, causing vortices near the boundary and even in the bulk interior as Po increases, which is fundamentally different from the phenomenon discovered in the rotating convection (Favier and Knobloch, 2020). Third, the topography does not always dampen the flow intensity. Under extremely strong Poincaré forcing, a sufficiently large barrier leads to a higher kinetic energy density in the modified cylinder than in the perfect cylinder. This suggests that boundary topography may exert a stronger influence on long lived planetary magnetic field than previously assumed.

It is worth pointing out that this study paves the way for a series of future explorations. In the currently reported work, the aspect ratio of the cylinder, Γ, is chosen to be at the primary resonance with the specific inertial mode $\boldsymbol{u}_{111}$ whose radial wave number is unity. For other resonant aspect ratios, the radial structure of such excited inertial modes could bring different types of topography-flow interplay. Especially, if the cylindrical geometry is not exactly at resonance with any particular mode, a large number of inertial modes will be excited, which might make the topographical effects even more complex. A second open question concerns the azimuthal modulation between terrain and flow. We by far have only set up a single topographical barrier on the cylindrical sidewall. It is necessary to extend the study to multiple-barrier cases or even general sidewall-topography cases. Last but not least, in geophysical problems such as the core dynamics, thermal convection and precession jointly play roles in driving core flows. How the terrain on core–mantle boundary or inner-outer core boundary affects core dynamics needs more numerical and experimental research.

Supplementary Materials

All multimedia views referenced in the main text are available at: https://pan.cstcloud.cn/s/bbcYIYumQ6s

Data Availability

The datasets generated and analyzed during the current study are too large to be publicly shared in online repositories. However, the data are available from the corresponding author upon request.

Author Contributions

Xiuyu Chen performed the numerical simulations, analysed the data, and wrote the first draft of the manuscript. Changshun Liu assisted with the numerical implementation and provided comments on the manuscript. Ligang Li co-conceived the study, supervised the work, and led the writing and revision. Dali Kong co-conceived the study, advised on the physical interpretation, and critically revised the manuscript. All authors approved the final version.

Acknowledgments

This work was supported by the National Natural Science Foundation of China (grant No. 12425306 and 12250013). This work made use of the High Performance Computing Resource in the Core Facility for Advanced Research Computing at Shanghai Astronomical Observatory.

References

Ascher, U. M., and Petzold, L. R. (1998). *Computer Methods for Ordinary*

Differential Equations and Differential-Algebraic Equations. Philadelphia: SIAM.

Chan, K. H., Li, L. G., and Liao, X. H. (2006). Modelling the core convection using finite element and finite difference methods. *Phys. Earth Planet. Inter.*, *157*(1–2), 124–138. https://doi.org/10.1016/j.pepi.2006.03.014

Chan, K. H., Zhang, K. K., and Liao, X. H. (2010). An EBE finite element method for simulating nonlinear flows in rotating spheroidal cavities. *Int. J. Numer. Methods Fluids*, *63*(3), 395–414. https://doi.org/10.1002/fld.2088

Chen, X. Y., Liu, C. S., Li, L. G., and Kong, D. L. (2025). A novel apparatus for rotating fluid experiments and newly discovered parameter space of triadic resonance in a rotating and latitudinal librating triaxial ellipsoid. *Res. Astron. Astrophys.*, *25*(11), 115020. https://doi.org/10.1088/1674-4527/ae04b6

Delplace, P., Marston, J. B., and Venaille, A. (2017). Topological origin of equatorial waves. *Science*, *358*(6366), 1075–1077. https://doi.org/10.1126/science.aan8819

Favier, B., and Knobloch, E. (2020). Robust wall states in rapidly rotating Rayleigh–Bénard convection. *J. Fluid Mech.*, *895*, R1. https://doi.org/10.1017/jfm.2020.310

Finke, K., and Tilgner, A. (2012). Simulations of the kinematic dynamo onset of spherical Couette flows with smooth and rough boundaries. *Phys. Rev. E*, *86*(1), 016310. https://doi.org/10.1103/PhysRevE.86.016310

Gao, D. L., Meunier, P., Le Dizès, S., and Eloy, C. (2021). Zonal flow in a resonant precessing cylinder. *J. Fluid Mech.*, *923*, A29. https://doi.org/10.1017/jfm.2021.574

Garcia, R., and Souriau, A. (2000). Inner core anisotropy and heterogeneity level. *Geophys. Res. Lett.*, *27*(19), 3121–3124. https://doi.org/10.1029/2000GL008520

Giesecke, A., Vogt, T., Gundrum, T., and Stefani, F. (2019). Kinematic dynamo action of a precession-driven flow based on the results of water experiments and hydrodynamic simulations. *Geophys. Astrophys. Fluid Dyn.*, *113*(1–2), 235–255. https://doi.org/10.1080/03091929.2018.1506774

Jiang, J. F., Kong, D. L., Zhu, R. X., and Zhang, K. K. (2015). Precessing cylinders at the second and third resonance: Turbulence controlled by geostrophic flow. *Phys. Rev. E*, *92*(3), 033007. https://doi.org/10.1103/physreve.92.033007

John, V. (2016). *Finite Element Spaces for Linear Saddle Point Problems*. Cham: Springer. https://doi.org/10.1007/978-3-319-45750-5

Kobine, J. J. (1995). Inertial wave dynamics in a rotating and precessing cylinder. *J. Fluid Mech.*, *303*, 233–252. https://doi.org/10.1017/S0022112095004253

Kong, D. L., Liao, X. H., and Zhang, K. K. (2014). The sidewall-localized mode in a resonant precessing cylinder. *Phys. Fluids*, *26*(5), 051703. https://doi.org/10.1063/1.4876924

Kong, D. L., Cui, Z., Liao, X. H., and Zhang, K. K. (2015). On the transition from the laminar to disordered flow in a precessing spherical-like cylinder. *Geophys. Astrophys. Fluid Dyn.*, *109*(1), 62–83. https://doi.org/10.1080/03091929.2014.976214

Lay, T., Williams, Q., and Garnero, E. J. (1998). The core-mantle boundary layer and deep earth dynamics. *Nature*, *392*(6675), 461–468. https://doi.org/10.1038/33083

Liao, X. H., and Zhang, K. K. (2012). On flow in weakly precessing cylinders: the general asymptotic solution. *J. Fluid Mech.*, *709*, 610–621. https://doi.org/10.1017/jfm.2012.355

Lin, Y. F., Noir, J., and Jackson, A. (2014). Experimental study of fluid flows in a precessing cylindrical annulus. *Phys. Fluids*, *26*(4), 046604. https://doi.org/10.1063/1.4871026

Manasseh, R. (1992). Breakdown regimes of inertia waves in a precessing cylinder. *J. Fluid Mech.*, *243*, 261–296. https://doi.org/10.1017/S0022112092002726

Meunier, P., Eloy, C., Lagrange, R., and Nadal, F. (2008). A rotating fluid cylinder subject to weak precession. *J. Fluid Mech.*, *599*, 405–440. https://doi.org/10.1017/S0022112008000335

Moffatt, H. K. (2014). Helicity and singular structures in fluid dynamics. *Proc. Natl. Acad. Sci. USA*, *111*(10), 3663–3670. https://doi.org/10.1073/pnas.1400277111

Pizzi, F., Giesecke, A., and Stefani, F. (2021a). Ekman boundary layers in a fluid filled precessing cylinder. *AIP Adv.*, *11*(3), 035023. https://doi.org/10.1063/5.0037922

Pizzi, F., Giesecke, A., Šimkanin, J., and Stefani, F. (2021b). Prograde and retrograde precession of a fluid-filled cylinder. *New J. Phys.*, *23*(12), 123016. https://doi.org/10.1088/1367-2630/ac3c0f

Rojas, R. E., Perevalov, A., Zürner, T., and Lathrop, D. P. (2021). Experimental study of rough spherical Couette flows: Increasing helicity toward a dynamo state. *Phys. Rev. Fluids*, *6*(3), 033801. https://doi.org/10.1103/PhysRevFluids.6.033801

Schöberl, J. (1997). NETGEN an advancing front 2D/3D-mesh generator based on abstract rules. *Comput. Visual. Sci.*, *1*(1), 41–52. https://doi.org/10.1007/s007910050004

Stenberg, R. (1984). Analysis of mixed finite element methods for the Stokes problem: A unified approach. *Math. Comput.*, *42*(165), 9–23. https://doi.org/10.2307/2007557

Vidal, J., Noir, J., Cébron, D., Burmann, F., Monville, R., Giraud, V., and Charles, Y. (2024). Geophysical flows over topography, a playground for laboratory experiments. *C. R. Phys.*, *25*(S3), 183–234. https://doi.org/10.5802/crphys.219

Whitford, R. (2004). *Fundamentals of Fighter Design*. Ramsbury: The Crowood Press Ltd.

Wood, W. W. (1966). An oscillatory disturbance of rigidly rotating fluid. *Proc. R. Soc. Lond. A Math. Phys. Sci.*, *293*(1433), 181–212. https://doi.org/10.1098/rspa.1966.0166

Zhang, K. K., and Liao, X. H. (2017). *Theory and Modeling of Rotating Fluids: Convection, Inertial Waves and Precession*. Cambridge: Cambridge University Press.